batteries

MDPI

Article

Single-Precursor Solid-Phase Synthesis of Poly(*o*-phenylenediamine) Sulfide Derivatives as Cost-Effective Organic Cathode Materials

Hanfei Luo †, Hao Zhang †, Rui Wang and Zhiping Song *

Hubei Key Lab of Electrochemical Power Sources, College of Chemistry and Molecular Sciences, Wuhan University, Wuhan 430072, China; 2023202030091@whu.edu.cn (H.L.); haozhang2035@whu.edu.cn (H.Z.); ruiwang1@whu.edu.cn (R.W.)

* Correspondence: zpsong@whu.edu.cn

† These authors contributed equally to this work.

Abstract

Organic cathode materials (OCMs) are widely regarded as promising candidates for sustainable rechargeable batteries; however, their practical application is hindered by insufficient electrochemical performance and a lack of scalable synthesis methods. Building on our previous study of poly(*o*-phenylenediamine) (PoPDA), we herein present a single-precursor, solid-phase synthesis of poly(*o*-phenylenediamine) sulfide derivatives (PoPDAS). Using *o*-phenylenediamine sulfide (oPDAS) as the sole precursor, thermal treatment at 300–350 °C triggers H_2SO_4 and its decomposition products to simultaneously drive oxidative polymerization forming a conjugated PoPDA backbone, and in situ sulfurization introducing polysulfide (–S_n–) linkages. The dual redox activity of C=N bonds in phenazine repeating units and S–S bonds in –S_n– linkages enables a high theoretical capacity, while the robust polymer matrix effectively confines soluble sulfur species during cycling. To optimize the trade-off between reversible capacity and long-term stability, a secondary sulfurization step has been implemented. Among fourteen samples prepared via varied synthetic routes and conditions, PoPDAS-B-350-0.5 with a moderate sulfur content of 27 wt% exhibits the best performance, delivering a reversible capacity of 358 mAh g^{-1} and 88% capacity retention after 800 cycles. Electrochemical analysis and ex situ characterization confirm the redox mechanism involving both C=N and S–S groups, and reveal the excellent cycling stability attributed to the robust polymer backbone that confines dissociated sulfur species. These results highlight the potential of integrating multiple redox-active moieties into a polymer architecture via a scalable solid-phase synthesis to afford practical OCMs.

Keywords: organic cathode materials; rechargeable lithium batteries; poly(*o*-phenylenediamine); disulfide; solid-phase synthesis

Academic Editor: Yong-Joon Park

Received: 4 June 2026
Revised: 6 July 2026
Accepted: 7 July 2026
Published: 9 July 2026

1. Introduction

While lithium-ion batteries currently dominate the energy storage landscape, their progress is increasingly hindered by energy density ceilings and the scarcity of critical metals like cobalt (Co) and nickel (Ni) [1–3]. Consequently, the development of high-energy-density cathode materials that are independent of transition metals and free from resource constraints is imperative. Organic cathode materials (OCMs), composed of earth-abundant elements such as carbon (C), hydrogen (H), oxygen (O), nitrogen (N), and sulfur (S), offer a novel paradigm to address this resource crisis [4]. Compared to traditional

inorganic counterparts based on transitional metals, OCMs not only boast structural tunability, environmental compatibility, and cost-effectiveness but also accommodate various ion systems (Li, Na, K, Mg, Zn) via their unique redox mechanisms, holding extensive application prospects [5–9]. In other words, although a newly developed OCM is typically first evaluated in a well-established Li battery system, it can be readily adapted to Na- or K-based systems, thereby reducing reliance on scarce metallic elements and enabling more sustainable battery technologies.

Over the past few decades, numerous n-type OCMs capable of cation insertion have been developed [10]. Whether in the form of small molecules or polymers, they typically incorporate redox-active functional groups such as carbonyl (C=O), imine (C=N), or disulfide (S–S) [11–13]. Small-molecule OCMs generally offer straightforward synthesis, well-defined molecular structures, and high theoretical specific capacities. However, their pronounced solubility in non-aqueous electrolytes often leads to poor cycling stability [14]. In contrast, polymeric OCMs exhibit significantly reduced—often negligible—solubility, which greatly enhances long-term electrochemical stability [15]. Nevertheless, polymeric materials face their own challenges, including complex synthetic routes, ill-defined molecular structures (due to limited solubility and difficulty in characterization), and lower theoretical capacities resulting from the incorporation of non-electroactive linking units [16–18]. Therefore, there is a pressing need to develop novel polymeric OCMs that combine facile and low-cost synthesis, high degrees of polymerization (to suppress dissolution), and a high density of redox-active groups to ensure high theoretical capacity.

In our previous work, we developed poly(*o*-phenylenediamine) (PoPDA) as a polymeric OCM based on C=N groups [19], and subsequently sulfurized it to obtain sulfurized poly(*o*-phenylenediamine) (SPoPDA) [20], a solid-phase conversion sulfur cathode material for lithium batteries. PoPDA was synthesized via oxidative polymerization of *o*-phenylenediamine (oPDA) monomer in glacial acetic acid using ammonium persulfate (APS) as the oxidant. SPoPDA was then prepared by further sulfurizing PoPDA with elemental sulfur (S_8) at 400 °C. Although all raw materials are low-cost and the sulfurization process is amenable to scale-up, the need for solution-based polymerization in PoPDA synthesis significantly hinders the large-scale production of SPoPDA. Another challenge lies in the electrochemical behavior of SPoPDA: while its high covalently bonded sulfur content (>50 wt%) endows the material with exceptional theoretical and practical capacities (>500 mAh g^{-1}), stable cycling relies on the solid-phase conversion of S–S bonds, a process typically facilitated only in ester-based electrolytes. This constraint inevitably leads to a low discharge plateau (typically ~1.7 V vs. Li^+/Li) and a large initial irreversible capacity loss (corresponding to low initial Coulombic efficiency, typically < 70%). The large irreversible capacity loss is primarily caused by parasitic reactions between dissolved sulfur species and carbonate solvents [21], which are necessary for forming a robust solid electrolyte interphase (SEI) that suppresses further active material dissolution [22].

To address the aforementioned challenges in both synthesis scalability and electrochemical performance, we herein propose an ingenious solid-phase, single-precursor synthesis of SPoPDA analogues—achieved simply by the pyrolysis of commercially available and low-cost *o*-phenylenediamine sulfate [oPDAS, $C_6H_4(NH_2)_2 \cdot H_2SO_4$]. Unlike conventional *o*-phenylenediamine (oPDA) monomer, the H_2SO_4 moiety in oPDAS serves as an intrinsic source of both oxidizing and sulfurizing agents. Upon heating, H_2SO_4 and its thermal decomposition products (e.g., SO_3, SO_2, and O_2) drive the oxidative polymerization of oPDA into PoPDA. Concurrently, elemental sulfur (S)—generated as a reduction product of sulfur-containing oxidants—reacts with the nascent polymer to introduce covalently bonded sulfur into the backbone. We designate the resulting material as PoPDAS, a name that ambiguously but conveniently reflects either "poly(*o*-phenylenediamine sulfate)" or

"poly(*o*-phenylenediamine) sulfide derivatives". This distinguishes it from our previously reported SPoPDA, which is prepared via a significantly different synthesis route and has a higher sulfur content. PoPDAS delivers a high reversible capacity arising from the dual redox activity of C=N and S–S groups, a feat enabled in ether-based electrolytes (in our prior work, ester-based electrolytes were found incompatible with C=N moieties, thereby suppressing their electrochemical utilization). Moreover, its robust, insoluble polymeric framework ensures excellent cycling stability and provides strong adsorption and confinement of potentially dissociative sulfur species during discharge–charge processes. To fully utilize this function and further boost capacity, we performed a secondary solid-phase sulfurization of the as-synthesized PoPDAS (Series A) using additional S_8, yielding samples with enhanced sulfur content (Series B). In parallel, to simplify the process into a single step, we also explored a one-pot synthesis by directly pyrolyzing a mixture of oPDAS and S_8 (Series C). However, this approach failed to reproduce comparable structures or electrochemical performance, likely because excess S_8 interferes with the oxidative polymerization of oPDA. In this work, we systematically investigate the synthesis, structural characteristics, and electrochemical behavior of all three PoPDAS series in rechargeable lithium batteries. The developed simple, low-cost, and self-sustaining solid-phase route establishes a novel synthetic paradigm for polymeric OCMs amenable to mass production. The excellent electrochemical performance validates our molecular design strategy of integrating an optimal amount of S–S bonds into robust polymer skeletons based on C=N (or similarly, C=O) redox centers. Collectively, this study offers significant insights into the rational development of cost-effective and scalable polymeric OCMs for practical energy storage applications.

2. Experimental Section

2.1. Materials and Reagents

All the raw materials and reagents were commercially purchased and used as received without further purification. The electrolyte of 1 M LiTFSI/G2 was prepared in-house in an argon-filled glovebox by dissolving the corresponding amount of lithium bis(trifluoromethanesulphonyl)imide (LiTFSI, 99.95%, Aldrich, St. Louis, MO, USA) into diglyme (G2, 98%, Adamas, Shanghai, China). *o*-Phenylenediamine sulfate (oPDAS, 97%) was purchased from Adamas (Shanghai, China). Ammonia monohydrate ($NH_3 \cdot H_2O$, 25–28 wt%), elemental sulfur (S_8, 99%) and toluene (99%) were obtained from Sinopharm (Shanghai, China).

2.2. Synthesis Procedures

Synthesis of PoPDAS-A-*x*. The PoPDAS-A-*x* series was synthesized via a direct sealed-tube heating method at varying temperatures of *x* °C (*x* = 250, 300, 350). In a typical procedure, 2 mmol (0.412 g) of oPDAS was placed in an ampoule, which was then evacuated, sealed, and heated at *x* °C for 12 h. Upon cooling to room temperature, a yellow oily byproduct was observed on the inner walls of the tube. The resulting solid was collected, finely ground, and dispersed in 0.2 M aqueous ammonia solution. The suspension was stirred at room temperature for 2 h to remove potentially incorporated sulfate (SO_4^{2-}) dopant ions. Subsequently, the solid was washed with deionized water until the filtrate was neutral, followed by successive washings with toluene and ethanol to remove potential elemental sulfur byproducts and soluble oligomers, respectively. The final precipitate was collected by vacuum filtration and dried under vacuum overnight at 80 °C, yielding a black powder designated as PoPDAS-A-*x*.

Synthesis of PoPDAS-B-*y*-*z*. The PoPDAS-B-*y*-*z* series was synthesized via the further thermal treatment of PoPDAS-A-300 with varying amounts of elemental S at

y °C (y = 300, 350). The parameter z represents the mass ratio of added elemental S to the PoPDAS-A-300 precursor (z = 0, 0.2, 0.5, 1.0), where the sample with z = 0 served as a control to evaluate the thermal stability of the precursor under further heating. In a typical procedure, 0.1 g of PoPDAS-A-300 and 0.1z g of elemental S were thoroughly mixed by grinding. The mixture was transferred into a 5 mL glass vial plugged with glass fiber and placed inside a small stainless steel (SS) vessel. The SS vessel was partially sealed using a fluorogel O-ring to minimize the leakage of vaporized sulfur while allowing the release of generated H_2S gas. Subsequently, the vessel was heated in a tube furnace at y °C for 6 h under a flowing nitrogen atmosphere, and the exhaust gas was passed through an aqueous NaOH solution to absorb H_2S. After cooling, the solid product was thoroughly washed with toluene to remove residual elemental S, followed by ethanol to remove the toluene. Finally, the product was dried under vacuum at 80 °C for 12 h to obtain a black powder designated as PoPDAS-B-y-z.

Synthesis of PoPDAS-C-x. The PoPDAS-C-x series was synthesized using the same procedure as for PoPDAS-A-x, except that elemental S was introduced via a one-pot approach. In a typical synthesis, 1 mmol (0.206 g) of oPDAS was thoroughly mixed with half the precursor's mass (0.103 g) of elemental S and sealed under vacuum in an ampoule tube. For x = 350, the mixture was heated at 350 °C for 12 h. For x = 300/350, the mixture was first heated at 300 °C for 6 h, followed by further heating at 350 °C for an additional 6 h. Post-treatment, including treatment with aqueous ammonia, sequential washing with deionized water, toluene, and ethanol, and vacuum drying, followed the same protocol as for PoPDAS-A-x, yielding a black powder designated PoPDAS-C-x.

2.3. Characterization Methods

Fourier-transform infrared (FT-IR) spectra were acquired using an ALPHA II spectrometer (Bruker, Ettlingen, Germany) in the form of KBr pellets. Raman spectra were obtained with a DXR2 Raman microscope (Thermo Fisher Scientific, Waltham, MA, USA) with a wavelength of 532 nm. X-ray diffraction (XRD) patterns were collected on a MiniFlex 600 diffractometer (Rigaku, Akishima, Japan) using Cu Kα_1 radiation (λ = 1.5406 Å) over a 2θ range of 5–75° at a scan rate of 10° min^{-1}. X-ray photoelectron spectroscopy (XPS) measurements were performed on a K-Alpha+ spectrometer (Thermo Scientific, Waltham, MA, USA) using monochromated Al Kα radiation (1486.6 eV). Elemental analysis (EA) was conducted using CHNS mode on a Vario UNICUBE elemental analyzer (Elementar, Frankfurt, Germany). Thermogravimetric (TG) analysis was performed on a STA 449 F3 (Netzsch, Selb, Germany) under a nitrogen atmosphere at a heating rate of 10 °C min^{-1}. Scanning electron microscopy (SEM) images were acquired on a MERLIN Compact microscope (ZEISS, Oberkochen, Germany).

2.4. Electrochemical Tests

Cathodes were prepared by a conventional doctor-blade coating method. In a typical procedure, 60 wt% active material (AM = PoPDAS), 30 wt% Ketjenblack conductive carbon (KB, EC-600JD), and 10 wt% polyvinyl alcohol (PVA) binder in deionized water were homogeneously mixed to form a slurry. The slurry was cast onto aluminum (Al) foil and dried under vacuum at 60 °C overnight. The resulting film was punched into circular discs (12 mm in diameter) with AM mass loading of ca. 1.2 mg cm^{-2}. For comparison, KB-only cathodes were prepared using the same procedure with a KB/PVA mass ratio of 9:1 and a KB mass loading of ca. 1.0 mg cm^{-2}. CR2025-type coin cells were assembled in an argon-filled glovebox ([O_2], [H_2O] $\leq$ 1 ppm) for all electrochemical measurements. Each cell consisted of a lithium foil anode and the aforementioned cathode separated by two stacked layers of Celgard 2325 membrane, and contained 60 µL of 1 M LiTFSI/G2 electrolyte.

All electrochemical measurements were carried out at room temperature within a voltage window of 1.0–3.8 V. Galvanostatic discharge–charge cycling and galvanostatic intermittent titration technique (GITT) measurements were performed using a CT-4008T battery testing system (Neware, Shenzhen, China). Unless otherwise stated, a current rate of 100 mA g^{-1} was applied. For GITT analysis, the 31st cycle of the galvanostatic discharge–charge test was modified by inserting a 2 h relaxation period following each 0.5 h discharge or charge pulse. Cyclic voltammetry (CV) and electrochemical impedance spectroscopy (EIS) were conducted on a PARSTAT MC electrochemical workstation (Princeton Applied Research, Oak Ridge, TN, USA). In CV measurements, the cell was successively cycled at scan rates of 0.1, 0.2, 0.5, and 1.0 mV s^{-1} (10 cycles per scan rate), and representative voltammograms were selected for analysis. EIS spectra were recorded at the fully charged state (3.8 V) during the first 50 galvanostatic cycles at 100 mA g^{-1}, over a frequency range of 10^5 to 10^{-2} Hz with an AC voltage amplitude of 10 mV.

2.5. Ex Situ Characterization

The pristine and electrochemically cycled PoPDAS-B-350-0.5 cathodes were harvested at selected states for ex situ XPS, EA, and SEM characterization. Specifically, after a given galvanostatic discharge–charge process (1.0–3.8 V, 100 mA g^{-1}), the coin cells were disassembled in an argon-filled glovebox. The cathode films were rinsed repeatedly with anhydrous tetrahydrofuran (THF) to remove residual electrolyte, and then dried under vacuum at 60 °C for 1 h. For comparison, the pristine cathode prior to cell assembly was directly subjected to the same characterization protocols. For XPS analysis, a 5 mm × 5 mm piece of the cathode film was cut and immediately sealed in an argon-filled aluminum-laminated pouch to minimize air exposure prior to measurement. To probe chemical changes within the active material beneath the solid electrolyte interphase (SEI), Ar^+ ion etching was applied to remove the surface layer to a depth of approximately 20 nm. All handling steps prior to XPS and SEM were performed inside the glovebox whenever possible to prevent contamination by ambient moisture or oxygen. For EA, to quantify sulfur speciation in the cathode composites, the discharged and recharged electrodes were first washed thoroughly with deionized water to dissolve and remove soluble Li_2S, followed by multiple rinses with ethanol. The samples were then dried under vacuum at 80 °C for 6 h. Finally, the active material layers (including that from the pristine electrode) were gently scraped off the Al foil and collected for EA measurements. For SEM analysis, the dried electrode films were cut into small pieces and mounted onto aluminum stubs with conductive carbon tape. All sample preparation steps prior to sputter coating were carried out in the glovebox to prevent air exposure.

3. Results and Discussion

3.1. Synthesis and Characterization

In our previous work, we successfully synthesized PoPDA via solution oxidative polymerization using oPDA, APS, and glacial acetic acid as the monomer, oxidant, and solvent, respectively. Despite the low cost of these raw materials and a relatively high product yield (~75%), the substantial consumption of organic solvent poses a significant obstacle to large-scale production. Consequently, we explored a solvent-free solid-phase synthesis of PoPDA and identified commercially available oPDAS as a promising single-source precursor (Figure 1a). In this system, the oPDA moiety serves as the essential monomer, while the H_2SO_4 moiety and its high-temperature decomposition products [23] (SO_3, SO_2, and O_2) function as in situ oxidants. The reaction byproducts likely include H_2O and S, originating from the eliminated protons of oPDA and the reduced sulfur species, respectively. At the polymerization temperature, the generated S may further react with

the nascent PoPDA to form sulfide derivatives, analogous to our previously reported two-step polymerization–sulfurization procedure used to prepare SPoPDA. The sulfurization byproduct, H_2S, can subsequently react with the remaining SO_2 to regenerate S, thereby sustaining the sulfurization process. Although this inevitable concurrent sulfurization precludes the formation of pristine PoPDA, it could be advantageous for the product's application as an OCM, as the introduced disulfide or polysulfide bonds can provide additional reversible capacity [24].

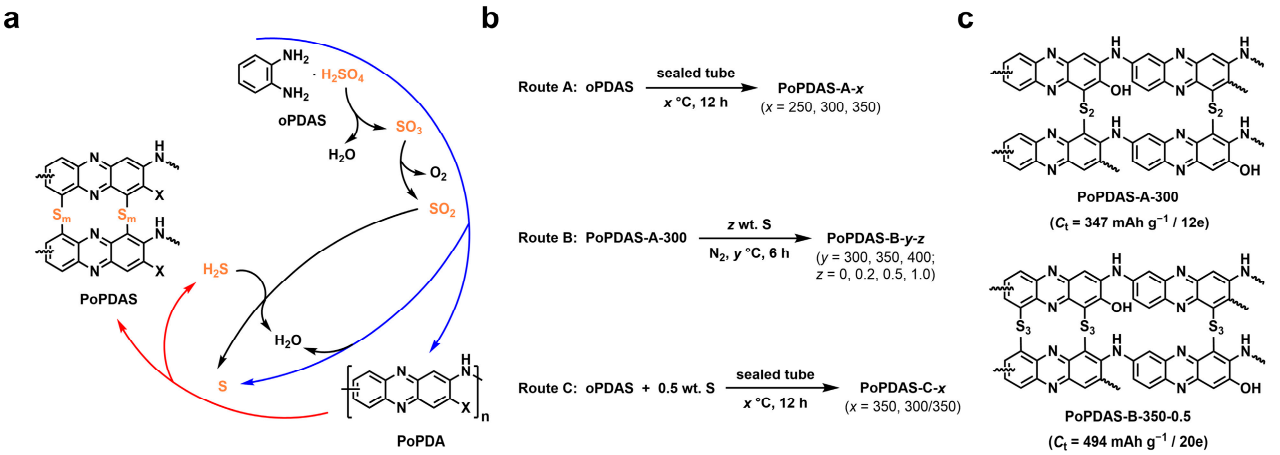

Figure 1. Synthesis of PoPDAS: (**a**) proposed synthetic mechanism for the conversion of oPDAS to PoPDAS (the X groups in PoPDA and PoPDAS denote structural uncertainties arising from the complex transformation reactions of the original $–NH_2$ terminals); (**b**) three different synthetic routes to PoPDAS; (**c**) proposed molecular structures of the representative materials derived from characterization results.

To systematically optimize the synthetic conditions and improve the electrochemical performance of the products, we adopted three synthetic routes to realize the above proposed hypothesis (Figure 1b; detailed synthetic conditions and yields are summarized in Table S1). In Route A, the oPDAS precursor was placed in a vacuum-sealed ampoule and heated at x °C (x = 250, 300, 350) for 12 h. The resulting products were washed sequentially with dilute ammonia, deionized water, toluene, and ethanol to remove potential doping anions (e.g., SO_4^{2-} or HSO_4^-), unreacted monomer, low-molecular-weight oligomers, and residual elemental S. After vacuum drying, the resulting black powder was designated as PoPDAS-A-x. To enhance the covalently bonded sulfur content in the polymer matrix and thus improve the reversible capacity, Route B was applied as a secondary sulfurization treatment. Specifically, the optimal material from Route A, PoPDAS-A-300, was homogeneously mixed with elemental S at z times its weight (z = 0, 0.2, 0.5, 1.0). The sample with z = 0 served as a control to evaluate the thermal stability of the precursor under further heating. The mixture was placed in a partially sealed vessel, and heated at y °C (y = 300, 350, 400) in a nitrogen atmosphere for 6 h. The post-synthesis treatment followed the same procedure as Route A, and the obtained products were designated as PoPDAS-B-y-z. To examine the feasibility of a one-step synthetic route yielding products similar to Series B, we also attempted Route C. This route was nearly identical to Route A but used a mixture of oPDAS and half its weight in elemental S (an optimal condition based on the results of Route B) as the precursor. The resulting materials were designated as PoPDAS-C-x, where x = 350 refers to heating at 350 °C for 12 h, and x = 300/350 refers to stepwise heating at 300 °C for 6 h followed by 350 °C for another 6 h, which may be more suitable for polymerization and sulfurization, respectively. For simplicity, the common prefix "PoPDAS-" in the above material names is omitted in many cases of the subsequent discussion.

The synthesis yields reflect the effects of polymerization and sulfurization, particularly within the same product series. To ensure a fair comparison across different series, the yield in Table 1 is defined as the ratio of the product mass to the theoretical mass of PoPDA (where X = NH_2 in Figure 1a) derived from the oPDAS monomer. For Series A-*x*, the yields are 32%, 94%, and 86% for *x* = 250, 300, and 350, respectively. These results indicate that a moderate reaction temperature of 300 °C is optimal; lower temperatures are insufficient to drive the oxidative polymerization, while higher temperatures may induce further pyrolysis of the nascent PoPDA. Subsequent electrochemical tests confirmed that A-300 exhibits the best performance among the three, and thus it was selected as the precursor for synthesizing Series B materials. To preliminarily examine the thermal stability of A-300 under further heating, it was pyrolyzed at 300, 350, and 400 °C. The product yields decreased from 94% for A-300 to 92%, 91%, and 76% for B-300-0, B-350-0, and B-400-0, respectively. Evidently, 300 °C and 350 °C are suitable for secondary sulfurization, whereas 400 °C is excessive and considerably degrades the original polymer matrix structure. For Series B-300-*z*, as *z* (the mass ratio of added elemental S to PoPDAS-A-300) increases from 0 to 0.2, 0.5, and 1.0, the yield gradually rises from 92% to 98%, 100%, and 105%. This verifies that at 300 °C, while a higher feed of elemental S enhances the extent of sulfurization, there is a diminishing return in its utilization. At an elevated temperature of 350 °C, the yields are notably higher compared to the analogues synthesized at 300 °C with the same *z* value (i.e., 101%, 105%, and 138% for *z* = 0.2, 0.5, and 1.0, respectively). This confirms that 350 °C is more effective for enhancing sulfurization efficiency, and the subsequent electrochemical tests demonstrated its slight superiority in improving electrochemical performance. For Series C, high yields of 145% and 152% were obtained for C-350 and C-300/350, respectively, indicating a high degree of sulfurization. However, distinct structural characterization results and significantly lower reversible capacities compared to those of Series A and B suggest a fundamentally different polymer matrix.

Table 1. Yield and elemental analysis of all synthesized PoPDAS samples.

Sample	Yield [a] (%)	Mass Fraction (wt%)					Molar Ratio of Atoms to Benzene Rings			
		C	H	N	S	O [b]	H	N	S	O [b]
A-250	32	62.3	3.3	18.7	11.2	4.5	3.82	1.54	0.40	0.33
A-300	94	62.4	2.4	18.7	13.2	3.3	2.80	1.54	0.48	0.24
A-350	86	62.5	2.1	18.3	14.4	2.7	2.38	1.50	0.52	0.19
B-300-0	92	62.2	2.2	18.4	12.7	4.5	2.53	1.52	0.46	0.33
B-350-0	91	62.3	2.4	18.5	12.9	3.9	2.78	1.53	0.47	0.28
B-400-0	76	63.1	2.3	18.1	10.7	5.8	2.60	1.48	0.38	0.42
B-300-0.2	98	54.8	1.7	16.3	24.5	2.7	2.19	1.53	1.00	0.22
B-300-0.5	100	52.9	1.6	15.7	26.3	3.5	2.14	1.53	1.12	0.30
B-300-1.0	105	52.0	1.4	15.2	27.8	3.6	1.88	1.50	1.20	0.31
B-350-0.2	101	53.5	1.8	16.1	24.7	3.9	2.41	1.55	1.04	0.33
B-350-0.5	105	53.5	1.9	15.2	26.9	2.5	2.51	1.47	1.13	0.21
B-350-1.0	138	46.9	1.7	13.5	34.9	3.0	2.58	1.49	1.68	0.29
C-350	145	48.4	1.4	14.2	30.9	5.1	2.08	1.50	1.44	0.47
C-300/350	152	48.3	1.5	14.6	32.5	3.0	2.26	1.56	1.51	0.28

a: The synthesis yield is defined as the ratio of the product mass to the theoretical mass of PoPDA (where X = NH_2 in Figure 1a) derived from the oPDAS monomer. b: The content of O is calculated by deducting the mass fractions of C, H, and N from 100%.

The fourteen synthesized PoPDAS samples listed in Table 1 were characterized using FT-IR and Raman spectroscopy, with the resulting spectra presented in Figure S1 and Figure S2, respectively. The FT-IR spectra show no significant variations among most samples, with the exception of the two Series C samples, which exhibit notable differences.

For Raman spectra, variations across all samples are negligible. These results confirm that the majority of the samples share a qualitatively similar molecular skeleton composed of the same functional groups. It is suggested that different synthesis temperatures and feed ratios of elemental sulfur primarily influence the relative abundance and distribution of these groups, particularly within the same sample series. For brevity, one representative sample from each series—A-300, B-350-0.5, and C-300/350—was selected for a detailed discussion of the characteristic FT-IR and Raman peaks.

Figure 2a displays the FT-IR spectra of the three selected samples, with the corresponding characteristic peak assignments detailed in Table S2. For samples A-300 and B-350-0.5, the weak doublet observed at ~3444 and ~3336 cm^{-1} is attributed to N–H stretching vibrations, confirming the presence of secondary amine structures within the polymer chains. The medium peak at ~1595 cm^{-1} and the strong peak at ~1448 cm^{-1} are assigned to C=N stretching and C=C skeletal vibrations, respectively [25]. These features provide evidence for the formation of phenazine moieties as repeating structural units and –NH– as linkages in the PoPDA polymer backbone. Due to the inherently low sensitivity of the S–S bond in FT-IR spectroscopy [26], only a subtle peak at ~465 cm^{-1} offers a clue regarding the polymer's sulfurization. Furthermore, the peak at ~756 cm^{-1}, corresponding to the out-of-plane bending vibration of C–H bonds in the benzene ring, shows a significant reduction in intensity for B-350-0.5 compared to A-300. This confirms that hydrogen atoms on the benzene rings were substantially substituted by sulfur atoms during secondary sulfurization. In contrast to A-300 and B-350-0.5, the spectrum of C-300/350 exhibits more pronounced differences, including red-shifted N–H and C=C peaks (by 11–32 cm^{-1}), a diminished C–H peak, and distinct patterns in the fingerprint region. These observations indicate a distinctly different molecular skeleton and a higher degree of sulfurization, which likely stem from the interplay between concurrently occurring oxidative polymerization and sulfurization in Route C. Figure 2b displays the Raman spectra of the three materials. Distinct characteristic peaks observed at ~1513 cm^{-1} and ~1386 cm^{-1} are attributed to the stretching vibrations of C=N and C–N bonds, respectively. These features corroborate the successful formation of the phenazine backbone. Furthermore, the presence of C–S and S–S bonds is verified by the signals appearing at ~666 cm^{-1} and ~476 cm^{-1}, respectively [26].

The thermal stabilities of the three samples were subsequently evaluated via TG under a nitrogen atmosphere (Figure 2c). A-300 and B-350-0.5 exhibit negligible mass loss below 200 °C, consistent with the FT-IR results indicating the absence of adsorbed water. Significant decomposition begins above 300 °C, accompanied by a gradual weight loss, ultimately yielding char residues of 71.4% and 65.7% at 800 °C, respectively. In contrast, C-300/350 displays a similar TG curve trend but exhibits significantly lower weight retention throughout the heating process, with a residual mass of only 48.4% at 800 °C. The thermal stability of the three samples, as indicated by their weight retention, shows a negative correlation with their sulfur content, the values of which were obtained from elemental analysis and will be reported later.

The crystal structures of the three representative materials were further investigated by XRD, as shown in Figure 2d. All samples exhibit only a broad, low-intensity peak, characteristic of a predominantly amorphous structure. However, C-300/350 displays a noticeable shift to a lower angle ($2\theta = 24°$) compared to A-300 and B-350-0.5 ($2\theta = 26°$). This shift suggests a distinct condensed-phase structure, likely arising from differences in the molecular architecture.

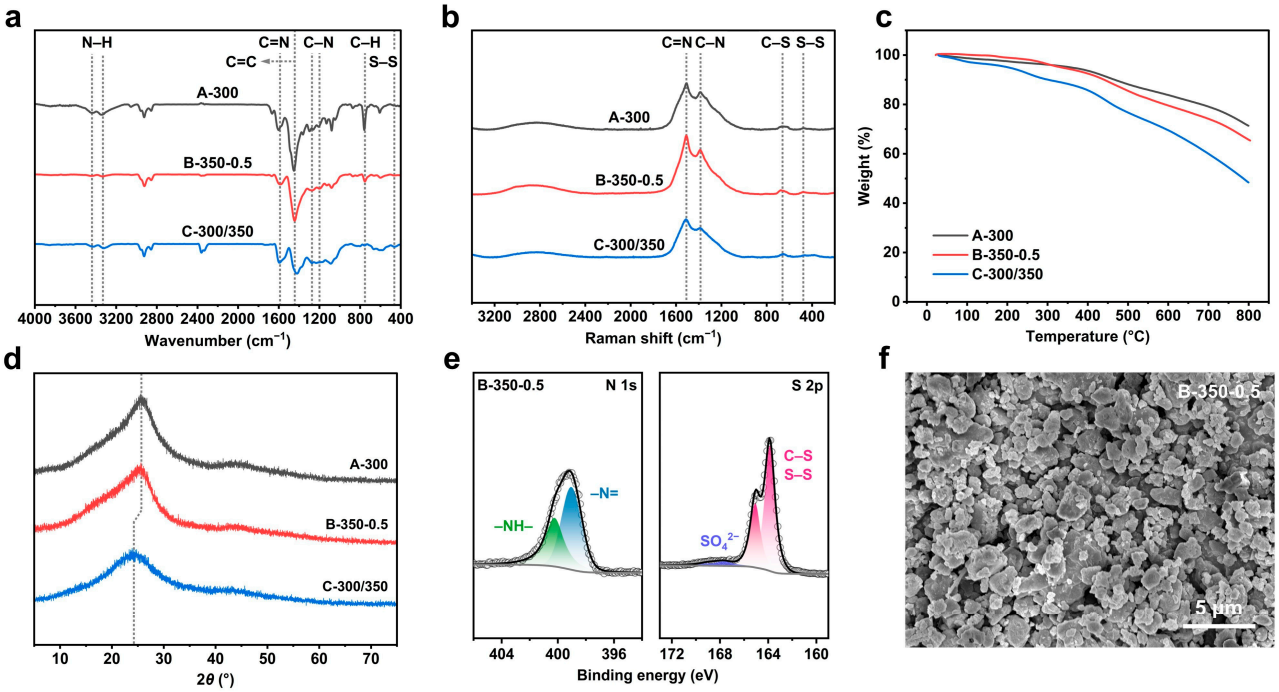

Figure 2. Structural characterization results of representative PoPDAS samples: (**a**) FT-IR spectra, (**b**) Raman spectra, (**c**) TG curves (in nitrogen atmosphere), and (**d**) XRD patterns of A-300, B-350-0.5, and C-300/350; (**e**) XPS spectrum and (**f**) SEM image of B-350-0.5.

Compared to the qualitative characterization methods discussed above, elemental analysis (EA) provides a more powerful approach for the quantitative assessment of the chemical composition and structure of the synthesized products. Table 1 summarizes the measured mass fractions of C, H, N, S, and O for all fourteen samples, where the O content was determined by difference. Given that the benzene ring is the most stable structural unit throughout the polymerization and sulfurization processes, we adopted it as a fundamental reference unit. Consequently, the molar ratios of H, N, S, and O atoms per benzene ring were calculated to simplify the analysis (Table 1). First, the N/benzene ratio for all samples was found to be approximately 1.5, rather than the expected value of 2 based on the stoichiometry of the oPDAS monomer. This suggests that the nascent $–NH_2$ terminal groups on the phenazine repeating units greatly disappeared, likely through hydrolysis into –OH groups via high-temperature vapor or deamination leading to direct coupling between benzene rings under high-temperature, highly oxidative conditions. The presence of –OH groups is further inferred from the O/benzene ratios ranging from 0.2 to 0.5, particularly since FT-IR spectra exclude the existence of absorbed H_2O, which could otherwise account for the O content. Second, the S/benzene ratios exhibit a distinct trend across and within the different sample series. For Series A, the ratio is relatively low, at 0.40–0.52. Following secondary sulfurization, this value increases to 1.00–1.20 for Series B-300 and 1.04–1.68 for Series B-350. A comparison of Series B-300 and B-350 samples reveals that the S/benzene ratios increase with both the amount of feed elemental S and the reaction temperature, a finding consistent with the trends observed in the aforementioned product yields. For Series C, the S/benzene ratio is 1.44–1.51, which is significantly higher than that of the Series B analogues prepared with the same amount of feed elemental S (B-*y*-0.5). Furthermore, the H/benzene and S/benzene ratios generally exhibit a trade-off relationship, although the larger error margin associated with measured H contents in EA may affect this interpretation. This observation aligns well with the substitution of S for H atoms during the sulfurization reaction.

Complementing the aforementioned analyses, additional XPS characterization was conducted for the optimal sample, B-350-0.5 (Figure 2e). The N 1s signal can be deconvoluted into two distinct components: –NH– and –N= species, centered at 400.3 and 399.0 eV, respectively. The S 2p spectrum is primarily dominated by C–S and S–S bonds, with the characteristic spin–orbit doublet peaks ($2p_{1/2}$ and $2p_{3/2}$) located at 163.9 and 165.1 eV, respectively. A minor signal observed at approximately 168 eV is attributed to trace residual sulfate (SO_4^{2-}) anions, likely acting as counterions for protonated amine terminals ($–NH_3^+$). These XPS findings corroborate the structural assignments derived from FT-IR, Raman, and elemental analysis.

Furthermore, SEM was utilized to examine the materials' microstructure. B-350-0.5 (Figure 2f) consists of irregularly shaped particles with primary sizes ranging from 0.5 to 2 μm, a morphology well-suited for achieving homogeneous mixing with conductive carbon in the electrode. By contrast, A-300 and C-300/350 (Figure S3) display markedly larger particle sizes (reaching ~5 μm and ~20 μm, respectively) along with a broader and less uniform size distribution.

Based on the aforementioned analysis, particularly the EA results, we propose plausible molecular structures for two representative samples, A-300 and its secondary sulfurization product B-350-0.5, as illustrated in Figure 1c. Both materials share an identical polymeric backbone comprising phenazine repeating units, amine (–NH–) linkages, and hydroxy (–OH) substituents. The primary structural distinction resides in the sulfur substitution sites and the length of the polysulfide ($–S_n–$) chains. Derived from the S/benzene molar ratios of 0.48 and 1.13, approximately 4 and 9 S atoms are deduced for every 4 phenazine units (equivalent to 8 benzene rings) in A-300 and B-350-0.5, respectively. These can be statistically assigned to two $–S_2–$ and three $–S_3–$ linkages, as depicted in Figure 1c. Considering the proposed molecular architectures and assuming a two-electron (2e) transfer capacity for each phenazine unit and S–S bond, the theoretical capacities of A-300 and B-350-0.5 are calculated to be 347 and 494 mAh g^{-1}, corresponding to 12e and 20e redox reactions, respectively. This calculation underscores the necessity of secondary sulfurization for enhancing the reversible capacity of the PoPDAS materials.

3.2. Electrochemical Performance

To evaluate the electrochemical performance of the fourteen PoPDAS samples as cathode materials in rechargeable batteries, we employed an electrode composition of AM/KB/PVA = 6:3:1 and utilized 1 M LiTFSI/G2 as the electrolyte. All electrochemical tests were conducted within a voltage window of 1.0–3.8 V. Initially, galvanostatic discharge–charge profiles for all samples were recorded at a current rate of 100 mA g^{-1}; the results are categorized into six groups (Figure 3a–f) to facilitate comparative discussion. In the following analysis, reversible capacity is defined as the maximum discharge capacity achieved during cycling, excluding the initial cycle, which may involve irreversible discharge capacity from reductive decomposition of the electrolyte. Additionally, capacity retention is defined as the ratio of the discharge capacity at a specified cycle number to the reversible capacity rather than that of the initial cycle. Notably, minor periodic oscillations are observed in the capacity curves of some samples, which can be attributed to ambient temperature fluctuations during cycling; however, these do not affect the overall long-term capacity retention trend.

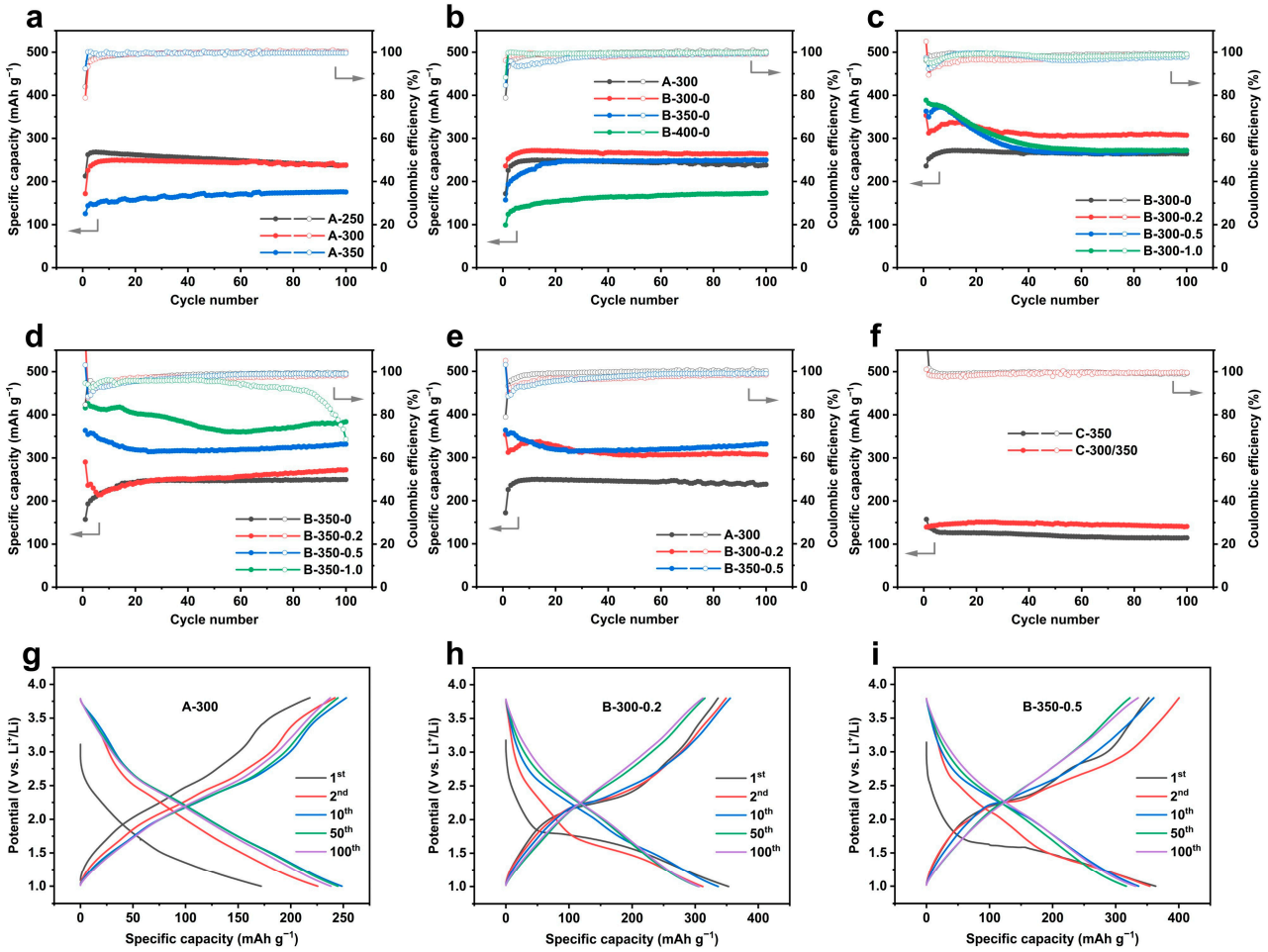

Figure 3. Comparison of electrochemical performance for PoPDAS samples (1.0–3.8 V, 100 mA g^{-1}): (**a**–**f**) cycling performance of (**a**) Route A products (A-*x*), (**b**) A-300 and its thermally treated products (B-*y*-0), (**c**) Route B products at 300 °C (B-300-*z*), (**d**) Route B products at 350 °C (B-350-*z*), (**e**) top-performing samples (A-300, B-300-0.2, and B-350-0.5), and (**f**) Route C products (C-*x*); (**g**–**i**) discharge–charge voltage profiles during cycling of (**g**) A-300, (**h**) B-300-0.2, and (**i**) B-350-0.5.

Figure 3a presents the electrochemical performance of the three Series A samples. Following a few initial activation cycles, A-250 and A-300 reach maximum discharge capacities of 268 and 250 mAh g^{-1}, respectively. After 100 cycles, both samples retain nearly identical capacities, 237 and 238 mAh g^{-1}, corresponding to capacity retentions of 88% and 95%, respectively. Coupled with their markedly different synthesis yields (32% for A-250 vs. 94% for A-300), this suggests that, despite their similar molecular structures, A-300 likely possesses a higher degree of polymerization, which contributes to its enhanced cycling stability. In contrast, A-350 delivers a significantly lower maximum discharge capacity of only 176 mAh g^{-1}, even though it exhibits excellent cycling stability. This implies that an excessively high reaction temperature may promote further pyrolysis of the polymeric framework, thereby compromising redox activity. Based on this analysis, A-300 was identified as the optimal material in Series A and was subsequently used both as the precursor for synthesizing Series B materials and as the benchmark for evaluating the electrochemical performance of other samples.

To introduce additional S–S bonds and thereby enhance reversible capacity, A-300 was further sulfurized to produce the Series B materials. As a preliminary step to assess the thermal stability of A-300 upon further heating and to identify an appropriate sulfurization temperature, A-300 was heated at different temperatures in the absence of elemental S, yielding the Series B-*y*-0 samples (where y = 300, 350, 400). Their electrochemical

performance is shown in Figure 3b and compared with that of the A-300 precursor. Overall, apart from the initial activation cycles, B-300-0 and B-350-0 exhibit reversible capacities and cycling stability comparable to those of A-300, with differences within 30 mAh g^{-1}. In contrast, B-400-0 delivers a significantly lower reversible capacity of 173 mAh g^{-1}, indicating substantial degradation of the polymer framework. This observation is consistent with its markedly reduced synthesis yield and lower S/benzene ratio relative to B-300-0 and B-350-0, as summarized in Table 1.

Subsequently, 300 °C and 350 °C were selected as the reaction temperatures for the secondary sulfurization of A-300, yielding the Series B-300-*z* and B-350-*z* materials, whose cycling performance is presented in Figure 3c,d. Within each series, increasing the amount of elemental S fed (denoted by *z*) into the reaction generally enhances the reversible capacity as expected. The highest capacities, 389 and 426 mAh g^{-1}, are achieved by B-300-1.0 and B-350-1.0, respectively. However, higher reversible capacity comes at the expense of cycling stability and Coulombic efficiency. Notably, B-350-1.0 exhibits a rapid decay in Coulombic efficiency before reaching 100 cycles. This underscores the need to strike a balance between capacity and stability by carefully tuning the S content in the polymer structure. This trade-off is chemically reasonable: a higher S content increases the average chain length ($n > 2$) in the $–S_n–$ moieties, thereby boosting discharge capacity. However, it also promotes the formation of dissociative sulfur species (e.g., Li_2S) during discharge. While the polymer matrix can confine these species to some extent, excessive amounts may overwhelmits encapsulation capacity, leading to active material loss and the polysulfide shuttle effect—ultimately resulting in capacity fading and reduced Coulombic efficiency, respectively. Among the two series, B-300-0.2 and B-350-0.5 represent optimal compromises, delivering reversible capacities of 337 and 358 mAh g^{-1} and capacity retentions of 91% and 93% after 100 cycles, respectively. Despite slightly reduced cycling stability and Coulombic efficiency compared to A-300, both exhibit significantly enhanced reversible capacities, as clearly illustrated in Figure 3e. These results suggest that a moderate S content of approximately 25%, corresponding to a S/benzene ratio of about 1.1 (Table 1), represents an optimal balance for regulating the structure of PoPDAS.

The cycling performance of the two Series C samples, C-350 and C-300/350, is presented in Figure 3f (with corresponding discharge–charge voltage profiles shown in Figure S4). Despite exhibiting reasonable cycling stability, both samples deliver significantly lower reversible capacities compared to the Series A and B materials, 139 and 151 mAh g^{-1}, respectively. This reduced capacity is unexpected given their notably higher S/benzene ratios (1.44 and 1.51), which would typically suggest enhanced theoretical capacity. The discrepancy is likely attributable to differences in their polymer backbone structure, which appears less defined and possibly redox-inactive, thereby contributing negligible electrochemical capacity. These results indicate that the current one-pot synthesis strategy for preparing high-sulfur-content PoPDAS has not yet been successful. Nevertheless, there remains considerable potential for improvement through further optimization of synthetic conditions, particularly once a clearer understanding of the underlying synthetic reaction mechanism is established (Figure 1a).

Figure 3g–i present the discharge–charge voltage profiles over cycling for three representative materials: A-300, B-300-0.2, and B-350-0.5. All exhibit an initial activation process over the first few cycles; therefore, the 10th cycle is selected as representative for analyzing their intrinsic electrochemical behavior. Generally, aside from differences in capacity, their representative discharge–charge curves show no significant distinctions: no distinct voltage plateaus are observed, and the profiles exhibit smooth, sloping curves across the entire voltage window of 1.0–3.8 V, particularly within the 1.0–3.0 V range. The average discharge voltages (at the 10th cycle) for A-300, B-300-0.2, and B-350-0.5 are 2.05,

1.92, and 1.99 V, respectively, indicating only minor variations among the three materials. Compared with A-300, B-300-0.2 and B-350-0.5 exhibit relatively larger overpotential during the first few cycles. This is likely attributed to the higher degree of sulfurization, which enhances cross-linking between polymer backbones and renders the material less accessible to electrolyte infiltration initially. After several discharge–charge cycles, however, the active material gradually swells as it becomes more thoroughly wetted by the electrolyte, eventually reaching a relatively stable state that facilitates reversible redox reactions.

When accounting for variations in testing conditions, the reversible capacity, voltage profiles, and cycling stability of A-300 agree well with those of our previously synthesized PoPDA prepared via solution polymerization. This consistency in electrochemical performance further supports the successful construction of the PoPDA framework using the solid-phase synthesis method. The two $–S_2–$ moieties present in the structure of A-300 (Figure 1c) do not appear to enhance reversible capacity, likely due to a trade-off between the increased number of redox-active electrons and the higher molecular weight of the repeating unit. In contrast, the structure of B-350-0.5 featuring three $–S_3–$ moieties (Figure 1c) demonstrates its superiority, achieving higher reversible capacity while maintaining relatively stable structural integrity during discharge–charge cycling. It should be noted that the reversible capacities of both A-300 and B-350-0.5 (250 and 358 mAh g^{-1}, respectively) remain significantly below their theoretical values (347 and 494 mAh g^{-1}). This gap becomes even more pronounced when the contribution from KB carbon is subtracted (based on a KB-only electrode delivering ~110 mAh g^{-1} as shown in Figure S5 and a KB-to-AM mass ratio of 1:2 in the composite electrode, the KB contribution is estimated at ~55 mAh g^{-1}). Beyond potential discrepancies between the idealized and actual molecular structures, a key limiting factor is the electrochemical stability window of the electrolyte, which restricts full utilization of the theoretical capacity. This is reflected in the continuously sloping voltage profile observed above 1.0 V, suggesting incomplete redox conversion. While integrating multiple electroactive C=N and S–S into a conjugated backbone substantially increases theoretical capacity, the electrostatic repulsion from already injected electrons may significantly lower the redox potential required for complete reduction of the molecule.

As the top-performing material among the fourteen samples, B-350-0.5 was selected for further electrochemical evaluation, as summarized in Figure 4. Figure 4a presents its rate capability, measured under a stepwise current-rate-increase protocol. Relative to the reversible capacity at 50 mA g^{-1}, B-350-0.5 retains 81%, 78%, 74%, and 69% at current rates of 100, 200, 500, and 1000 mA g^{-1}, respectively, demonstrating excellent rate performance. Furthermore, Figure 4b illustrates the long-term cycling stability of B-350-0.5. At a current rate of 100 mA g^{-1}, it delivers a discharge capacity of 327 mAh g^{-1} after 200 cycles, corresponding to a capacity retention of 91%. At an elevated current rate of 500 mA g^{-1} (preceded by three activation cycles at 100 mA g^{-1}), the material maintains a capacity of 245 mAh g^{-1} after 800 cycles, representing 88% retention relative to its reversible capacity of 279 mAh g^{-1} (measured at the 4th cycle). Together, these results confirm that B-350-0.5 exhibits among the best cycling stability reported to date for OCMs with comparable reversible capacities.

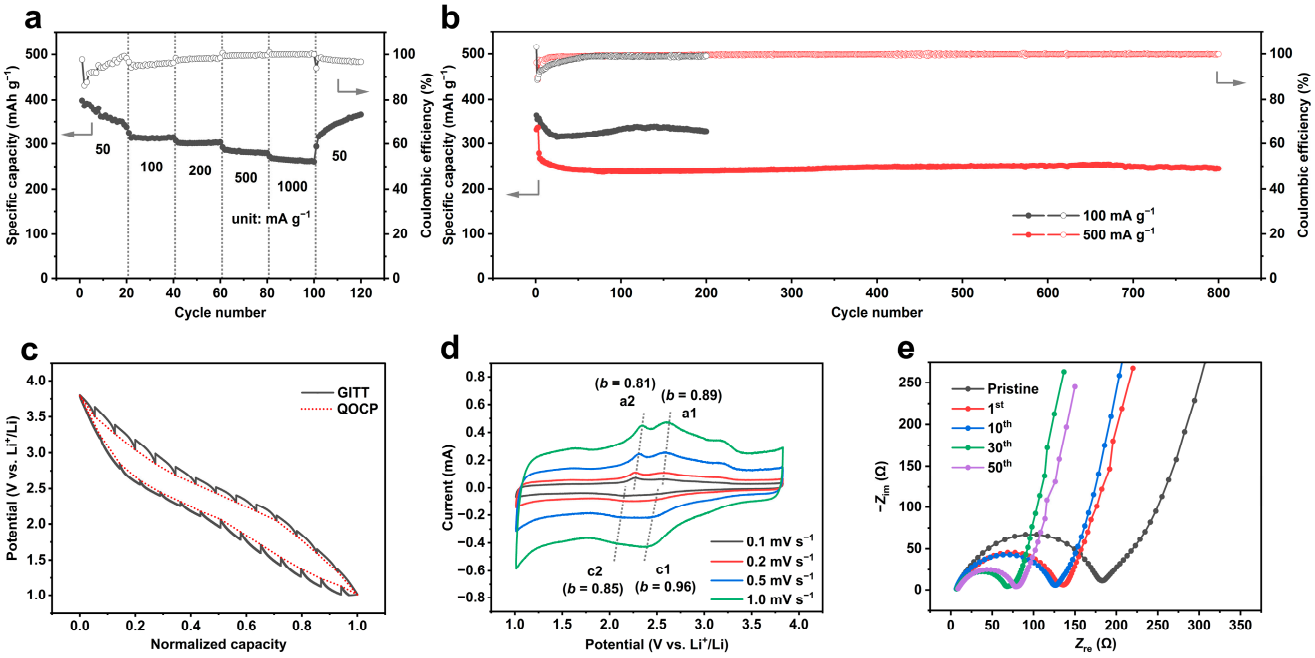

Figure 4. Electrochemical performance of the optimal sample PoPDAS-B-350-0.5: (**a**) rate performance at current rates ranging from 50 to 1000 mA g^{-1}; (**b**) long-term cycling performance at 100 and 500 mA g^{-1}; (**c**) GITT and QOCP curves at the 31st cycle of galvanostatic discharge–charge at 100 mA g^{-1} (with 2 h relaxation following each 0.5 h discharge or charge step); (**d**) typical CV curves at scan rates of 0.1, 0.2, 0.5, and 1.0 mV s^{-1}; (**e**) EIS Nyquist plots of the charged-state cell during cycling at 100 mA g^{-1}. The voltage range for all tests was 1.0–3.8 V.

Figure 4c presents the typical GITT curve and the corresponding quasi-open-circuit potential (QOCP) profile of B-350-0.5. The voltage hysteresis between discharge and charge is approximately 0.5 V, which primarily arises from the equilibrium potential gap (~0.35 V) and, to a lesser extent, from kinetic overpotentials during discharge and charge (~0.07 V each). This notable disparity suggests that the electrochemical reduction and reoxidation of PoPDAS proceed via somewhat different reaction pathways. To further probe the reaction kinetics, CV measurements were carried out on B-350-0.5 (Figure 4d). Despite significant peak overlap, two pairs of redox peaks—centered at approximately 2.6/2.5 V and 2.3/2.2 V at slow scan rates—remain discernible in the CV curves. A linear fit of the peak currents (i_p) vs. scan rates (v) (Figure S6) yields b-values of 0.96, 0.85, 0.89, and 0.81 for redox peaks c1, c2, a1, and a2, respectively. These b-values close to 1 indicate that the electrochemical response of the B-350-0.5 electrode is predominantly pseudocapacitive in nature, which supports its excellent rate capability observed in Figure 4a.

To investigate the evolution of the electrode state during cycling, EIS measurements were performed on cells employing the B-350-0.5 cathode in both the pristine and charged states. The corresponding Nyquist plots are shown in Figure 4e, while the equivalent circuit model and detailed fitting parameters used for quantitative analysis of the impedance components are summarized in Table S3. The pristine electrode exhibits a charge transfer resistance (R_{CT}) of 183 Ω, which decreases significantly to 136 Ω after the first cycle and further gradually declines to 68 Ω by the 30th cycle. This trend correlates well with the substantial reduction in overpotential observed after the initial cycle, as reflected in the discharge–charge voltage profiles (Figure 3i), where the overpotential decreases progressively in subsequent cycles. The continuous decline in R_{CT} is attributed to enhanced electrolyte infiltration into the polymeric active material, facilitated by the swelling of the polymer during discharge. This swelling is driven by Li^+ insertion and electrostatic repulsion among negatively charged moieties. By the 50th cycle, R_{CT} increases only slightly

to 78 Ω, indicating that the electrode structure reaches a relatively stable state after an initial self-accommodation process, thereby enabling long-term cycling stability (Figure 4b).

3.3. Electrochemical Redox Mechanism

To elucidate the electrochemical redox mechanism of B-350-0.5, as a representative sample of PoPDAS, various ex situ characterization techniques, including XPS, EA, and SEM, were performed on electrodes harvested at distinct states: pristine, discharged to 1.0 V, and recharged to 3.8 V. As shown in Figure 5a, the XPS N 1s spectra reveal that upon discharge, the peak intensity corresponding to the imine group (–N=) at 399.0 eV decreases markedly, accompanied by the emergence of a new component at 398.3 eV, which is assigned to the –NLi– moiety. In the S 2p spectra, the signals associated with C–S/S–S bonds (163.9 eV for S $2p_{3/2}$; binding energies hereinafter refer to S $2p_{3/2}$ unless otherwise noted) observed in the pristine electrode shift predominantly to lower binding energies after discharge, giving rise to peaks at 163.1 eV assigned to C–SLi and 161.6 eV assigned to Li_2S. Additionally, minor features appear at higher binding energies, 169.7 eV and 167.7 eV, which can be reasonably attributed to Li_2SO_4 and Li_2SO_3, respectively, as decomposition products of the LiTFSI [$LiN(SO_2CF_3)_2$]-based electrolyte [27,28]. In the N 1s and S 2p spectra of the discharged electrode, the residual signals corresponding to the –N= and C–S/S–S moieties confirm the incomplete reduction of the redox-active groups, supporting our earlier explanation for the discrepancy between the practical and theoretical capacities. In the Li 1s spectra, a pronounced peak emerges at 56.1 eV after discharge, consistent with the formation of –NLi–, C–SLi, and Li_2S species. However, due to overlapping binding energies, these contributions cannot be deconvoluted with high precision. Following the subsequent charge to 3.8 V, the N 1s, S 2p, and Li 1s spectral features almost fully revert to those of the pristine state, demonstrating excellent redox reversibility. Nevertheless, a residual trace of Li_2S remains detectable in the S 2p spectrum, suggesting that a small fraction of the discharged Li_2S product fails to be re-oxidized back to $–S_n–$ moieties. This incomplete recovery is likely attributable to the poor electronic and ionic conductivities of Li_2S. Such irreversible accumulation of Li_2S is probably responsible for the slight capacity fading observed during the initial cycles of Series B materials (Figure 3c,d). Based on the above analysis, we can draw a clear conclusion: both the C=N bonds in the phenazine units of the polymer backbone and the S–S bonds in the side-chain $–S_n–$ linkages contribute to the reversible capacity and exhibit high reversibility during the discharge–charge process.

To gain a more quantitative understanding of the reaction mechanism, particularly the evolution of sulfur species, we performed EA on electrodes at the three different states. In contrast to the ex situ XPS protocol described above, the discharged and recharged electrodes were thoroughly rinsed with water to completely remove Li_2S and other potentially soluble sulfur species. This washing protocol ensures that only sulfur atoms covalently bound to the polymer backbone remain in the electrode (although C–SLi moieties may undergo hydrolysis to form C–SH), while dissociative or non-covalently bound sulfur species are effectively eliminated. Consequently, the sulfur content measured by EA reflects exclusively the fraction of fixed (i.e., backbone-integrated) sulfur, and the fraction of dissociative sulfur can be derived by a difference method. Since N originates solely from the PoPDAS active material and its total elemental content remains invariant during the discharge–charge process, the N content serves as a reliable internal reference. Thus, the S/N atomic ratio can be used as a quantitative indicator of the relative change in covalently bound sulfur during electrochemical cycling. The CHNS-mode EA results for the pristine, discharged, and recharged electrodes are summarized in Table S4 (for the pristine state, the B-350-0.5 powder data from Table 1 were used directly, as the S/N atomic ratio remains

unchanged upon electrode fabrication). From these data, the corresponding S/N atomic ratios were calculated and presented in Figure 5b: 0.77 for the pristine electrode, decreasing to 0.47 after discharge, and largely restored to 0.72 upon recharge. Based on these values, we estimate the atomic ratio of dissociative sulfur to fixed sulfur in the discharged state to be approximately 0.39. This value is in reasonable agreement with the theoretical ratio of 0.33 predicted by our proposed molecular structure for B-350-0.5 (Figure 1c). The incomplete recovery of the S/N ratio after charging is consistent with the XPS results, which also indicate residual Li_2S remaining in the electrode (Figure 5a).

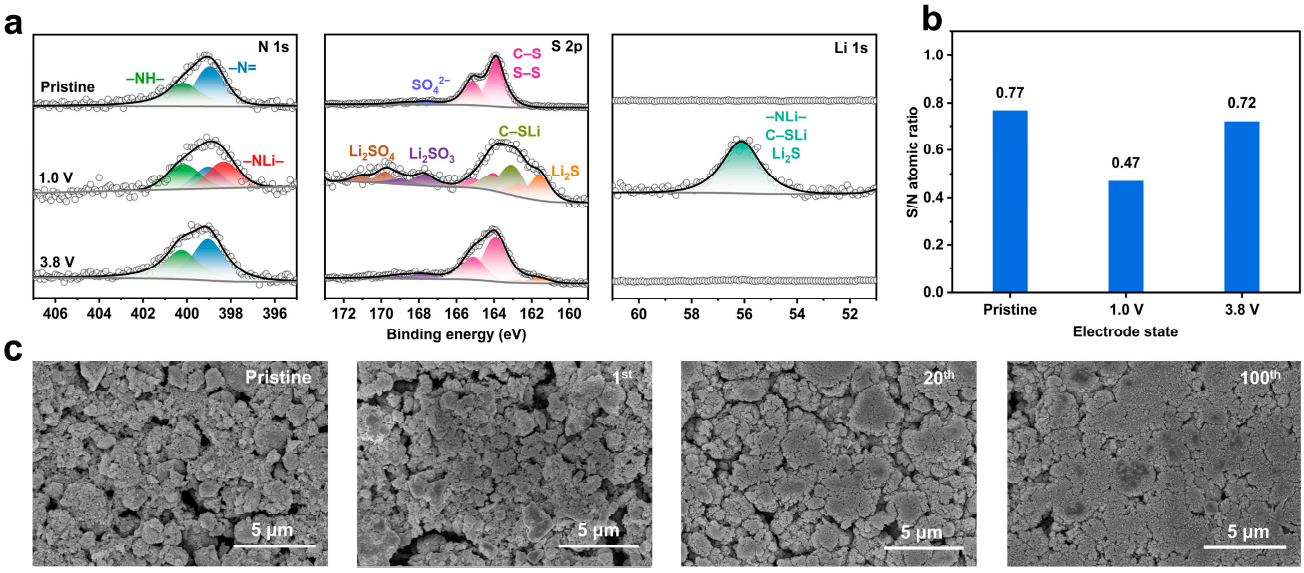

Figure 5. Ex situ characterization of PoPDAS-B-350-0.5 electrodes at different charge/discharge states (1.0–3.8 V, 100 mA g^{-1}): (**a**) XPS spectra at pristine, discharged (1.0 V), and recharged (3.8 V) states; (**b**) S/N atomic ratios derived from elemental analysis of the above three electrodes (after removing Li_2S); (**c**) SEM images of charged-state electrodes during cycling.

To investigate the morphological evolution of the PoPDAS electrodes during discharge–charge cycling, SEM images of electrodes at various cycle numbers were recorded (Figure 5c). The pristine electrode exhibits a loosely agglomerated morphology. Throughout cycling, the electrode maintains good structural integrity, with no obvious voids or cracks—features that would typically indicate active material dissolution. This observation underscores the effective confinement of sulfur species by the polymer matrix. Such morphological stability is a key factor contributing to the electrode's excellent long-term cycling performance (Figure 4b).

4. Conclusions

In summary, we have developed a single-precursor, solid-phase synthesis of poly(*o*-phenylenediamine) sulfide derivatives (PoPDAS) and demonstrated their use as high-performance OCMs for rechargeable lithium batteries. Using oPDAS as the sole precursor, the oPDA moiety can be oxidatively polymerized into a PoPDA backbone by the H_2SO_4 moiety and its decomposition products at appropriate heating temperatures. Concurrently, elemental S generated as a byproduct induces an in situ sulfurization reaction, introducing polysulfide (–S_n–) linkages into the polymer backbone. A secondary sulfurization treatment further enhances the sulfur content, thereby increasing the theoretical capacity. Three synthetic routes were explored, yielding fourteen samples for systematic optimization of reaction conditions. Among these, PoPDAS-B-350-0.5, which contains a moderate sulfur content of 27 wt%, achieves an optimal balance between reversible capacity (358 mAh g^{-1})

and long-term cycling stability (88% capacity retention after 800 cycles). Various electrochemical techniques (GITT, CV, EIS) and ex situ characterization methods (XPS, EA, SEM) were employed to investigate the redox mechanism and the origin of the cycling stability. The excellent electrochemical performance stems from the synergistic redox activity of both the C=N bonds in the phenazine units of the polymer skeleton and the S–S bonds within the $–S_n–$ linkages, coupled with the effective confinement of soluble sulfur species by the robust polymer matrix during discharge–charge cycling. The outstanding electrochemical performance of PoPDAS among reported OCMs highlights the great potential of molecular design strategies that integrate redox-active C=N (or C=O) and S–S functionalities within a single material framework. Moreover, the simplicity and scalability of this novel solid-phase synthesis method pave the way for large-scale production, facilitating the practical implementation of OCMs in rechargeable batteries.

Supplementary Materials: The following supporting information can be downloaded at: https://www.mdpi.com/article/10.3390/batteries12070247/s1, Figure S1: FT-IR spectra of all synthesized PoPDAS samples; Figure S2: Raman spectra of all synthesized PoPDAS samples; Table S1: Synthetic conditions and yields of the three routes to PoPDAS; Table S2: Characteristic FTIR band (cm^{-1}) assignments of A-300, B-350-0.5, and C-300/350 (corresponding to Figure 2a); Figure S3: SEM images of (a) A-300 and (b) C-300/350; Figure S4: Discharge–charge voltage profiles during cycling of Route C products (1.0–3.8 V, 100 mA g^{-1}): (a) C-350; (b) C-300/350; Figure S5: Typical discharge–charge voltage profiles of KB electrode (1.0–3.8 V, 100 mA g^{-1}); Figure S6: Relation between $lg(i_p)$ and $lg(v)$, where i_p and v refer to the peak currents and scan rates of CV curves in Figure 4d, respectively; Table S3: Fitted parameters of elements in the below equivalent circuit for the EIS data of Li–B-350-0.5 cell (corresponding to Figure 4e); Table S4: Elemental analysis of B-350-0.5 electrodes at different states. (corresponding to Figure 5b).

Author Contributions: H.L.: Methodology, Investigation, Data curation, Visualization, Formal analysis, Writing—original draft, Writing—review & editing; H.Z.: Methodology, Data curation, Writing—original draft, Writing—review & editing; R.W.: Investigation, Formal analysis; Z.S.: Conceptualization, Methodology, Funding acquisition, Project administration, Supervision, Writing—review & editing. All authors have read and agreed to the published version of the manuscript.

Funding: This research was funded by the National Key Research and Development Program of China (2022YFB2402201) and the National Natural Science Foundation of China (Nos. 21975189, 22179102, and 22379115).

Data Availability Statement: The original contributions presented in the study are included in the article/Supplementary Materials.

Acknowledgments: We acknowledge the Shiyanjia Lab (www.shiyanjia.com (accessed on 6 July 2026)) for support of EA and XPS characterizations, Core Research Facilities of CCMS (WHU) for access to SEM characterizations. During the preparation of this manuscript, the authors used Qwen 3.0 for the purposes of language polishing. The authors have reviewed and edited the output and take full responsibility for the content of this publication.

Conflicts of Interest: The authors declare no competing financial interest.

References

1. Kim, H.; Kim, J.C. Opportunities and challenges in cathode development for non-lithium-ion batteries. *eScience* **2024**, *4*, 100232. [CrossRef]
2. Niu, H.; Zhang, N.; Lu, Y.; Zhang, Z.; Li, M.; Liu, J.; Zhang, N.; Song, W.; Zhao, Y.; Miao, Z. Strategies toward the development of high-energy-density lithium batteries. *J. Energy Storage* **2024**, *88*, 111666. [CrossRef]
3. Pol, V.G. Lithium-Ion Battery Critical Materials Sustainability. *ACS Energy Lett.* **2025**, *10*, 2553–2558. [CrossRef]

4. Cao, R.; Qian, J.; Zhang, J.-G.; Xu, W. Organic Cathode Materials for Rechargeable Batteries. In *Rechargeable Batteries: Materials, Technologies and New Trend*; Zhang, Z., Zhang, S.S., Eds.; Springer International Publishing: Cham, Switzerland, 2015; pp. 637–671.
5. Zhao, Y.; Zhou, M.; Zeng, X.; Yang, J.; Wang, J.; NuLi, Y. High-Performance Magnesium-Organic Batteries Enabled by a Multielectron Redox-Bipolar Polyaniline Cathode. *Adv. Funct. Mater.* **2025**, *35*, 2423533. [CrossRef]
6. Masese, T.; Kanyolo, G.M. Advancements in cathode materials for potassium-ion batteries: Current landscape, obstacles, and prospects. *Energy Adv.* **2024**, *3*, 60–107. [CrossRef]
7. Zhang, Y.; Li, M.; Li, Z.; Lu, Y.; Li, H.; Liang, J.; Hu, X.; Zhang, L.; Ding, K.; Xu, Q.; et al. A High Capacity p-Type Organic Cathode Material for Aqueous Zinc Batteries. *Angew. Chem. Int. Ed.* **2024**, *63*, e202410342. [CrossRef]
8. Zhang, H.; Gao, Y.; Liu, X.-H.; Yang, Z.; He, X.-X.; Li, L.; Qiao, Y.; Chen, W.-H.; Zeng, R.-H.; Wang, Y.; et al. Organic Cathode Materials for Sodium-Ion Batteries: From Fundamental Research to Potential Commercial Application. *Adv. Funct. Mater.* **2022**, *32*, 2107718.
9. Lu, Y.; Zhang, Q.; Li, F.; Chen, J. Emerging Lithiated Organic Cathode Materials for Lithium-Ion Full Batteries. *Angew. Chem.* **2023**, *135*, e202216047.
10. Innocenti, A.; Adenusi, H.; Passerini, S. Assessing n-type organic materials for lithium batteries: A techno-economic review. *InfoMat* **2023**, *5*, e12480. [CrossRef]
11. Guo, Q.; Xu, H.; Chu, X.; Huang, X.; Yu, M.; Feng, X. Structural codes of organic electrode materials for rechargeable multivalent metal batteries. *Chem. Soc. Rev.* **2025**, *54*, 4035–4086. [CrossRef] [PubMed]
12. Wang, D.-Y.; Guo, W.; Fu, Y. Organosulfides: An Emerging Class of Cathode Materials for Rechargeable Lithium Batteries. *Acc. Chem. Res.* **2019**, *52*, 2290–2300. [CrossRef] [PubMed]
13. Wang, H.; Yao, C.-J.; Nie, H.-J.; Wang, K.-Z.; Zhong, Y.-W.; Chen, P.; Mei, S.; Zhang, Q. Recent progress in carbonyl-based organic polymers as promising electrode materials for lithium-ion batteries (LIBs). *J. Mater. Chem. A* **2020**, *8*, 11906–11922. [CrossRef]
14. Zou, S.; Jiang, D.; Liu, Y.; Peng, C.; Zhou, L.; Zhang, W.; Luo, D.; Huang, H.; Wang, H.; Ji, S.; et al. Multifunctional binder on inhibiting dissolution of small-molecule organic electrode materials for Li-Ion batteries and Na-ion batteries. *J. Alloys Compd.* **2025**, *1035*, 180907. [CrossRef]
15. Yin, M.; Zhou, X.; Xue, Z. Challenge and Design Strategies of Polymer Organic Electrodes for Lithium-Ion Batteries. *Macromol. Chem. Phys.* **2024**, *225*, 2300427. [CrossRef]
16. Zhao, C.; Yan, J.; Ma, Z.; Zhang, Y.; Hu, T.; Zhang, H. Recent advances in conjugated ladder-type porous polymer networks for rechargeable batteries. *Chem. Synth.* **2025**, *5*, 32. [CrossRef]
17. Liu, Y.; Niu, Z.; Dai, G.; Chen, Y.; Li, H.; Huang, L.; Zhang, X.; Xu, Y.; Zhao, Y. Phenothiazine-based copolymer with redox functional backbones for organic battery cathode materials. *Mater. Today Energy* **2021**, *21*, 100812. [CrossRef]
18. Li, L.; Yin, Y.-J.; Hei, J.-P.; Wan, X.-J.; Li, M.-L.; Cui, Y. Molecular Engineering of Aromatic Imides for Organic Secondary Batteries. *Small* **2021**, *17*, 2005752. [CrossRef]
19. Zhang, X.; Li, G.; Wang, J.; Chu, J.; Wang, F.; Hu, Z.; Song, Z. Revisiting the Structure and Electrochemical Performance of Poly(o-phenylenediamine) as an Organic Cathode Material. *ACS Appl. Mater. Interfaces* **2022**, *14*, 27968–27978. [CrossRef] [PubMed]
20. Wang, Q.; Zhang, X.; Wang, J.; Chu, J.; Li, M.; Huang, L.; Hu, Z.; Wang, Y.; Song, Z. Sulfurized poly(o-phenylenediamine) as a novel high-performance solid-phase conversion sulfur cathode. *Chem. Eng. J.* **2023**, *471*, 144402. [CrossRef]
21. Yim, T.; Park, M.-S.; Yu, J.-S.; Kim, K.J.; Im, K.Y.; Kim, J.-H.; Jeong, G.; Jo, Y.N.; Woo, S.-G.; Kang, K.S.; et al. Effect of chemical reactivity of polysulfide toward carbonate-based electrolyte on the electrochemical performance of Li–S batteries. *Electrochim. Acta* **2013**, *107*, 454–460. [CrossRef]
22. He, B.; Rao, Z.; Cheng, Z.; Liu, D.; He, D.; Chen, J.; Miao, Z.; Yuan, L.; Li, Z.; Huang, Y. Rationally Design a Sulfur Cathode with Solid-Phase Conversion Mechanism for High Cycle-Stable Li–S Batteries. *Adv. Energy Mater.* **2021**, *11*, 2003690. [CrossRef]
23. Corgnale, C.; Gorensek, M.B.; Summers, W.A. Review of Sulfuric Acid Decomposition Processes for Sulfur-Based Thermochemical Hydrogen Production Cycles. *Processes* **2020**, *8*, 1383. [CrossRef]
24. Cui, S.; Li, T.; Tao, D.; Zhang, D.; Cao, Y.; Xu, F. Disulfide bonded polyimide cathode of rechargeable magnesium batteries: Improved capacity via reversible break/formation of disulfide and sulfur-oxygen bonds. *Energy Storage Mater.* **2024**, *71*, 103672. [CrossRef]
25. Sun, T.; Li, Z.-J.; Yang, X.; Wang, S.; Zhu, Y.-H.; Zhang, X.-B. Imine-Rich Poly(o-phenylenediamine) as High-Capacity Trifunctional Organic Electrode for Alkali-Ion Batteries. *CCS Chem.* **2019**, *1*, 365–372. [CrossRef]
26. Kiani, R.; Steimecke, M.; Alqaisi, M.; Bron, M.; Sebastiani, D.; Partovi-Azar, P. Characterization of sulfur/carbon copolymer cathodes for Li–S batteries: A combined experimental and ab initio Raman spectroscopy study. *RSC Adv.* **2023**, *13*, 27756–27763. [CrossRef] [PubMed]

27. Soria-Fernández, A.; Castillo, J.; Cid, R.; Song, Z.; Wu, H.; Carriazo, D.; Armand, M.; Zhang, H.; Santiago, A. Beyond the Hype: Decoding Bis(fluorosulfonyl)imide Chemistry in Advanced Lithium-Sulfur Batteries. *Small Methods* **2026**, *10*, e02084. [CrossRef] [PubMed]
28. Diao, Y.; Xie, K.; Xiong, S.; Hong, X. Insights into Li-S Battery Cathode Capacity Fading Mechanisms: Irreversible Oxidation of Active Mass during Cycling. *J. Electrochem. Soc.* **2012**, *159*, A1816. [CrossRef]